Research Article Vol. 6, No. 5 / May 2019 / Optica 668

Enhanced luminescence in rare-earth-free fast-sintering glass-ceramic

V. Fuertes,[1,*] J. F. Fernández,[1] and E. Enríquez[2]

[1]Department Electrocerámica, Instituto de Cerámica y Vidrio, CSIC, Kelsen 5, 28049, Madrid, Spain
[2]Centro Tecnológico Vidres, S.L., Ctra. Onda, Km 3.4, 12540 Villareal, Castellón, Spain
*Corresponding author: vfuertes@icv.csic.es

Received 5 February 2019; revised 18 March 2019; accepted 1 April 2019 (Doc. ID 359612); published 16 May 2019

One of the major challenges pursued in the luminescent materials community is to develop rare-earth-free phosphors in order to reduce the use of rare-earth elements, because of the lack of their availability and the environmental problems derived from their mining and processing. In this work, a rare-earth-free glass-ceramic-based phosphor with high photoluminescence has been designed. This novel phosphor rich in Na-rich plagioclase feldspar crystallizations presents high crystallinity, ∼94%, and a dual micro-nanostructure provided by a fast-sintering processing route. Structural disorder in Si–Al distribution favors formation of luminescent centers in the glass-ceramic material, which results in an enhancement of both the UV–blue and the red luminescence regarding natural feldspars, 1 order of magnitude and 6 times, respectively. A microstructural and structural study by means of x-ray diffraction, Raman spectroscopy, scanning electron microscopy, transmission electron microscopy (TEM), high-resolution TEM, cathodoluminescence, and nuclear magnetic resonance evidence the important role of composition in the alteration of Si–Al ordering schemes. A strong correlation between Si–Al disorder and the presence of active luminescent centers is corroborated. Our research shows a sustainable, cost-effective, innovative, and scalable material that may be considered as an alternative to rare-earth phosphors for applications such as security markers or light-emitting glasses. This novel family of rare-earth-free glass-ceramics opens a new gate through structural tailoring to enhance and tune the intrinsic luminescent emissions displayed for relevant future optical applications.

https://doi.org/10.1364/OPTICA.6.000668

1. INTRODUCTION

The development of luminescent inorganic materials has been subject of extensive research in past years because these materials present interesting properties, a good stability, and may be industrially produced in large quantities, which make them suitable for applications in devices involving the artificial production of light [1]. Luminescence is a property strongly affected by several factors such as crystallinity, active centers, the host composition, and the interactions between each other [2]. A wide variety of luminescent centers has been considered in semiconductors and insulating materials, such as rare-earth and transition-metal ions, excitons or donor–acceptor pairs among others. Despite that most inorganic phosphors are doped with rare-earth elements and have importance in modern electronic technology, the negative environmental impact of rare-earth mining and processing, the scarcity of these elements, and the control by China of the world's rare-earth element market lead to the need for finding alternative novel rare-earth-free-doped phosphors [3].

Silicate host lattices have been considered in last years to obtain efficient luminescent emissions, which is mainly motivated because of their stiff nature [4]. Other host lattices considered have been fluoride, oxyfluorides, garnets, nitrides, and oxynitrides [5,6]. In this context, glass and glass-ceramic materials are suitable to synthetize these luminescent matrices [7], since they have a large potential for many applications in the field of photonics. Glass and glass-ceramics are highlighted by their low-cost, large-volume production, and easy shapeability. However, one of the main drawbacks of glass regarding its luminescence behavior is the presence of many point defects that generate trapping sites responsible for nonradiative recombinations, causing the light yield to be usually lower regarding crystals [8,9]. In contrast, glass-ceramics may be synthetized with higher crystallinity, reducing such a problem. Glass-ceramics for optical applications are easy and flexible to manufacture, and are more cost efficient than corresponding single crystals. In glass-ceramics, higher optical quality, higher doping concentrations, and materials larger in size and with more complex shapes can be achieved [10].

In nature, there are materials that also exhibit luminescence, as the case of feldspars, a group of rock-forming tectosilicate minerals that constitute as much as 60% of the Earth's crust. Luminescence in feldspars has been used in mineralogy for different purposes, such as quantitative separation of different mineral species, for the evidence of different mineral generations, zonation of crystals, or to establish textural relationships between minerals, among others [11]. The most common luminescence phenomena

used to study minerals have been thermoluminescence (TL), photoluminescence (PL), and cathodoluminescence (CL). The emission bands in feldspars are mainly related to structural defects (mainly Al-O$^-$-Al, Si-O$^-$-Si) as well as activator elements incorporated in the feldspar structure like Ti^{3+}, Fe^{3+}, Eu^{2+}, Eu^{3+}, Ce^{3+}, or Sm^{3+}, among others [12]. Nevertheless, although natural feldspars exhibit noticeable luminescence and are well-known, synthetic feldspar matrices have scarcely been studied in the literature for such purposes because of the difficulties to synthesize such structures without secondary phases [4].

Within feldspar minerals, one of the most abundant groups is plagioclase feldspars, solid solutions between albite ($NaAlSi_3O_8$) and anorthite ($CaAl_2Si_2O_8$) feldspars. The framework of albite consists of rings of four tetrahedra, where each tetrahedron is centered by a Si^{4+} or an Al^{3+}, cation with a Si^{4+}/Al^{3+} ratio of 3:1. Each oxygen atom is located at the corners of each tetrahedron and links two tetrahedra. In contrast, anorthite has also rings of four tetrahedra having a Si^{4+}/Al^{3+} ratio of 1:1. Albite has four symmetrically nonequivalent sites, designated as $T_1(0)$, $T_1(m)$, $T_2(0)$, and $T_2(m)$. In the most ordered state, known as low albite, Al^{3+} cations are placed in $T_1(0)$ positions, but as disorder increases, Al^{3+} cations migrate to the other three positions. In intermediate plagioclases, as anorthite content increases, replacement of Na^+ and Si^{4+} by Ca^{2+} and Al^{3+} increases regarding a pure albite, in order to obtain the local charge balance. This replacement modifies the Si–Al ordering and favors the formation of defects such as Al–O–Al bonds [13], one of the main luminescent centers in feldspars [11].

Due to problems related to use of rare-earth elements, it is an appealing challenge in our society to obtain materials that may be able to act as phosphors without activation of rare-earth elements. All of this motivates the first-time study, to the best of authors' knowledge, of a synthetic material that may have a wide spectral luminescence because of the presence of structural defects and possible modulation by the incorporation of different nonrare-earth activator elements in the plagioclase structure.

In recent years, development of nanotechnology and nanoscience has allowed the improvement and creation of new materials with unique properties [14]. In nanosized particles, unique luminescence properties have been revealed, which might be quite different from their bulk counterparts [15]. Glass-ceramics having uniformly dispersed crystals <100 nm in size provide unique attributes for current products and are promising for new applications [16]. Luminescent properties are strongly influenced by microstructure, crystallite, and particle size of the material under study [17]. Thus, luminescence seems to be an interesting property to study in a novel glass-ceramic with dual micro-nanostructural characteristics, and relevant insulator, optical, and thermal behavior [18,19].

In this context, the aim of this work is to evaluate the luminescent behavior, mainly intrinsic luminescence produced by structural defects, of a novel rare-earth-free glass-ceramic obtained by the fast-sintering process, which was carried out by PL and CL techniques. A thorough analysis of the structural defects involved in such emissions by deconvolution of emission curves will allow establishing the relevance of the synthetized feldspar structure. Luminescence emissions were compared with a natural sodium aluminosilicate. For this purpose, x-ray diffraction (XRD) patterns, Raman spectroscopy measurements, and scanning electron microscopy (SEM) micrographs are presented. Moreover, transmission electron microscopy (TEM) and high-resolution TEM (HRTEM) images are presented in order to analyze in detail the micro-nanostructure of the glass-ceramic host. Finally, nuclear magnetic resonance (NMR) measurements are presented to evince the important role of composition in the alteration of Si–Al ordering schemes and the generation of Si–Al disordered distribution.

2. EXPERIMENTAL PROCEDURE

A. Sample Preparation

The glass-ceramic was prepared by a conventional ceramic process as described in previous works [18]. The precursors used were kaolin with a particle size $d_{50} = 5.34$ μm, and frit in a weight proportion of 10/90, respectively. The frit and kaolin compositions expressed in term of equivalent oxides are shown in Table 1. Precursors were mixed by milling in an alumina ball mill for 20 min with 37 wt. % of water. Then, the mixture was dried at 60°C for 24 h and sieved using a mesh of 100 μm. The dried and sieved mixture possesses monomodal particle size distributions with $d_{50} = 6.72$ μm. Disk samples 2 cm in diameter of mixture powder were pressed at 39.2 MPa. Pressed samples were thermally treated in an industrial furnace at 1220°C for 6 min with a 30° C min^{-1} heating rate, in a fast-sintering cycle that comprises a total time of 55 min. The key component to obtain a Na-rich plagioclase structure is Sr^{2+}, which is a lattice disruptor that favors the formation of the sodium-rich (Na-rich) aluminosilicate after devitrification process, even though the frit just presents a 2.68% of Na_2O. Moreover, a Na-rich mineral sample (commercial product, Feldspar ASM-100 with ref. AM601.797) was selected for having a similar structural composition, in order to compare their luminescence properties. For optical applications, materials need to be shaped, which usually requires a thermal treatment. Thus, a Na-rich mineral sample was thermally treated at 1220°C for 6 min with a 30° C min^{-1} heating rate, in order to compare its luminescence with the glass-ceramic developed in this work.

B. Characterization

Structural characterization was carried out at long and short range by XRD and solid-state magic-angle spinning (MAS) NMR, respectively, on the powders obtained by milling the sintered samples at room temperature. XRD patterns were recorded over the angular range 10–70° 2θ by using an x-ray diffractometer Bruker

Table 1. Chemical Composition of the Glass-Ceramic and the Natural Na-Rich Feldspar, Expressed as wt. % of Equivalent Oxides

Oxides wt. %	Frit	Kaolin	Natural Na-Rich Feldspar
SiO_2	51.63	55.49	69.25
ZrO_2	–	–	–
SrO	8.05	–	0.02
Na_2O	2.68	–	10.44
K_2O	1.46	1.21	0.20
Al_2O_3	21.14	42.48	19.27
ZnO	1.10	–	–
CaO	10.47	0.18	0.51
B_2O_3	1.40	–	–
P_2O_5	0.84	0.04	0.02
MgO	1.04	0.10	0.05
BaO	–	–	0.07
Fe_2O_3	0.12	0.43	0.14
TiO_2	0.09	0.07	0.03

D8 Advance with Cu Kα radiation, 40 kV, and 40 mA in order to identify the crystalline phases formed. The identification of the crystalline phases was carried out by comparison with the corresponding JCPDS cards. The crystalline phases and the glassy phase content were calculated by the diffraction software Bruker's Diffrac. Eva, through the integration of the areas corresponding to the amorphous and crystalline contribution.

^{29}Si MAS NMR spectra were recorded on a Bruker AV-400-WB spectrometer equipped with 4 mm MAS probe and operating at 79.49 MHz by a simple pulse of $\pi/2$ at 50 KHz. A relaxation time of 60 s, spectral width of 40 kHz, and 2 h of accumulation time with a spinning rate of 10 kHz were taken. Kaolin (–91.2 ppm) was used as secondary reference with respect to tetramethylsilane (TMS) as primary reference.

Microstructural characterization was studied by means of field emission SEM (FESEM), using a Hitachi S-4700. Polished samples were chemically etched with 5 vol. % of hydrofluoric acid (HF) with the aim of removing the glassy phase and revealing the microstructure.

TEM was performed at 200 keV on Philips Tecnai F20. HRTEM images were also acquired to study the local crystalline quality. Electron diffraction pattern and diffraction pattern simulations after fast Fourier transform (FFT) of HRTEM images were also used. For TEM measurements, samples were prepared in the cross section by standard sample preparation methods, carrying out a mechanical thinning and argon ion milling to attain the required electron transparency.

The PL measurements were carried out at room temperature with a spectrofluorometer (Fluorolog-3, HORIBA Jobin Yvon). The luminescence intensity was measured over the wavelength range 330–700 nm using a xenon arc lamp as an excitation source (λexc ¼ 380 nm). Samples were measured in front-face mode, with an integration time of 0.1 s. Density of the grating used was 1200 (blaze, 500), the side entrance/exit bandpass was 2.00 nm, and the spot of the source was 1 cm × 0.3 cm. The CL images were acquired with a CL spectrometer (Gatan Mono CL3) attached to a SEM (Fei Inspect) with a cooling system with liquid N_2 and spectral expansion up to the infrared. The excitation for CL measurements was provided at 30 kV electron beam in low-vacuum mode. CL spectra were accumulated in a single-shot mode within an exposure rate of 2 nm s^{-1}. All the CL spectra were taken at room temperature. The whiteness and CIE L*a*b* coordinates, the most common uniform color space, were measured by a colorimeter Konica Minolta, Spectra Magic NX, with Color Data Software CM-S100w. L* measures from white to black (0–100), a* measures from green to red, and b* measures from blue to yellow.

3. RESULTS AND DISCUSSION

A. Luminescent Response Associated with the Micro-Nanostructure: a Correlation for Glass-Ceramic

Figure 1 depicts the PL behavior at room temperature of fast-sintered glass-ceramic in comparison with the PL of the thermally treated Na-rich feldspar mineral. The raw Na-rich feldspar mineral was also evaluated, but it does not present luminescence due to structural defects (further analysis in Fig. S1 in Supplement 1), as occurs in the thermally treated samples. This fact might be probably due to high Si–Al order in tetrahedral sites, as will be discussed later. The excitation spectra [Figs. 1(a) and 1(c)] of both samples register two bands: a broad band centered at 322 nm for both materials and a sharp one at 355 nm for the

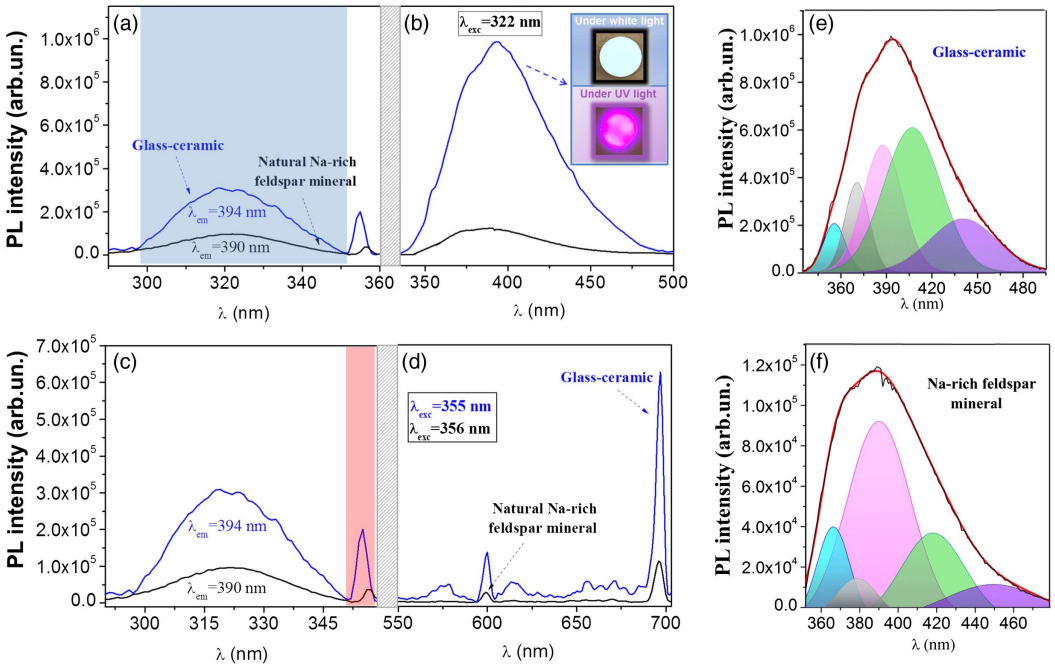

Fig. 1. Enhancement of photoluminescence in glass-ceramic in comparison with thermally treated (TT) Na-rich feldspar mineral. Room-temperature photoluminescence spectra in 1220 °C, 6 min thermal-treated glass-ceramic (blue) and in a Na-rich feldspar mineral TT (black): (a), (c) excitation spectra under λ_{em} = 394 nm for glass-ceramic material and λ_{em} = 390 nm for the Na-rich feldspar mineral TT; (b) UV–blue emission spectra for λ_{exc} = 322 nm [blue highlighted band in (a)]; (d) emission spectra in the range 550–700 nm [red highlighted band in (c)] under λ_{exc} = 355 nm and 356 nm for glass-ceramic and Na-rich feldspar mineral TT, respectively; and (e), (f) deconvolution of UV–blue emission for glass-ceramic and Na-rich feldspar mineral TT, respectively. Each defect-related emission is associated with the same color in order to make easier the comparison between each.

glass-ceramic and at 356 nm for the Na-rich feldspar mineral. The band at 322 nm is the most intense for both materials, and it corresponds to intrinsic luminescence, related to defects of feldspar structure, while the second one is mainly related to transitions undergone by iron impurities. Therefore, thermal treatment favors the structural-reorganization-inducing defects responsible for the observed luminescence. Exciting the first band at an absorption wavelength of 322 nm, the UV–blue emission was measured and plotted for both materials in Fig. 1(b). This emission is the typical UV–blue emission [20] characteristic of feldspar minerals, and it shows a PL intensity measured of 1 magnitude order higher in the glass-ceramic regarding the thermally treated Na-rich feldspar mineral used as reference. As well, a redshift from 390 nm to 394 nm was noticed for the novel rare-earth-free glass-ceramic of this work. In the inset of Fig. 1(b), two photographs of a glass-ceramic sample are shown. The upper image shows the glass-ceramic under white light excitation, which evinces their whiteness, making it suitable for being used as glaze in ceramic tile or as a white pigment in polymer-based applications. The bottom image under UV light excitation reveals the great luminescence emission of this synthetic rare-earth-free phosphor. The color observed is slightly pinkish ($L^*(C) = 65.71$, $a^*(C) = 37.28$, and $b^*(C) = -16.36$) because of the combination of UV–blue and red emission, since excitation was carried out with a UV source with some spectral width.

Under $\lambda_{exc} = 355$ nm for the glass-ceramic and $\lambda_{exc} = 356$ nm for the thermally treated mineral, the second band of Fig. 1(c) was excited, and the correspondent emission was plotted in Fig. 1(d). In this case, emission spectra are dominated by red emission, centered at 697 nm and 696 nm for the glass-ceramic and the thermally threated mineral, respectively, and this is attributed to Fe^{3+} emissions. The red luminescence in alkali feldspars occurs when a Fe^{3+} ion occupies Al^{3+} tetrahedral sites in the feldspar structure [11], and a ${}^4T1 \rightarrow {}^6A1$ transition of Fe^{3+} takes place. For ordered alkali feldspar, Fe^{3+} should substitute Al^{3+} in T_{10} positions. In the case of disordered feldspars, T_{1m}, T_{20}, and T_{2m} position would also be substituted, but in lesser extent than that of T_{10} sites, if a total disorder does not exist. After signal deconvolution of all lluminescence emissions, Figs. 1(e) and 1(f), their assignments, and the relative intensity of emission bands between glass-ceramic and mineral feldspar are summarized in Table 2. Regarding PL intensity, the most intense red emission, at about 696–697 nm, is 6 times higher in the glass-ceramic and it may correspond to Fe^{3+} on tetrahedral sites [21,22], as it has been discussed. Besides, some small emissions are found in the glass-ceramic in the range 656–685, which are probably caused by Fe^{3+} ions located at $T_1(m)$, $T_2(0)$, and $T_2(m)$ tetrahedral positions [23], which suggest that some degree of disorder in Si–Al distribution might occur. The differences in Fe^{3+} site occupancy together with alteration in the local crystalline field due to variations in chemical composition strongly influence the position and intensity of this peak [11,24]. These Fe^{3+}-related emissions have their origin in the presence of Fe_2O_3 in the precursors, both frit and kaolin, as it can be seen in Table 1. In order to check that iron oxide is presented in the glass-ceramic after sintering, an energy dispersive x-ray (EDX) analysis and x-ray fluorescence (XRF) are carried out (see Fig. S2, Tables S1 and S2 in Supplement 1). In addition, quartz emissions are found in the range 578–656 nm.

In the 335–500 nm range, feldspar emissions can be deconvoluted in five emission bands, which may be mainly attributed to $[AlO_4/alkali^+]$ or $[AlO_4]^0$ defects, and Al-O^--Al centers, according to Table 2. The first two types of defects are caused when Al^{3+} ion substitutes Si^{4+}, and then a positive charge is necessary to maintain local charge balance. If the positive charge is an alkali cation placed in adjacent positions to Al^{3+} cations, the center formed will be $[AlO_4/alkali^+]$, while if a hole is trapped, the resulting center will be an $[AlO_4]^0$ [20,22]. In the case of Al-O^--Al centers, also known as Löwenstein bridges, they are the most common structural defect in feldspars, and they occur, typically in the range 400–480 nm, when an oxygen hole center is adjacent to two Al^{3+} cations, one of them structural and the other one an Al^{3+} impurity [22,26–29]. This emission might also be related to Ti centers, whose corresponding emissions occur when Ti^{4+} is incorporated as Ti^{3+} in Al-sites, forming Al-O^--Ti bridges [26,29]. Both emission centers have been proposed in the bibliography as the origin of the blue luminescence in feldspars. In the case of a sodic plagioclase, substitution of Na^+ and Si^{4+} by Ca^{2+} and Al^{3+} take place regarding albite structure, which generate some Si–Al disorder and the formation of Al-O^--Al linkages, $[AlO_4/alkali^+]$ and $[AlO_4]^0$ centers might be favored [13].

Table 2. PL Emission Peaks, Excitation Wavelength (First Wavelength Corresponds to the Glass-Ceramic While the Second One to the Thermally Treated Mineral), Intensity Ratios, and Peak Assignments for Glass-Ceramic and Thermally Treated Mineral Feldspar Peaks

$\lambda_{glass\text{-}ceramic}$ (nm)	$\lambda_{mineral\ TT}$ (nm)	λ_{exc} (nm)	$I_{glass-ceramic}/I_{mineral\ TT}$	Assignment
356	366	322	4.5	quartz emission [25]
371	379	322	18.1	$[AlO_4/alkali^+]$ or $[AlO_4]^0$ [20,22]
388	390	322	5.4	$[AlO_4/alkali^+]$ or $[AlO_4]^0$ [20,22]
410	418	322	14.1	Al-O^--Al center [2627–28]
440	450	322	12.7	Al-O^--Al center [29,26]
578	–	355–356	–	oxygen vacancies in quartz [30]
600	599	355–356	4.9	quartz emission [25,31]
614	615	355–356	9.5	nonbridging oxygen hole center in quartz [32]
615	609	322	11.6	nonbridging oxygen hole center in quartz [32]
656	–	355–356	–	nonbridging oxygen hole center in quartz [32]
663	–	355–356	–	Fe^{3+} impurities on tetrahedral sites [23]
671	670	355–356	6.9	Fe^{3+} impurities on tetrahedral sites [23]
676	–	355–356	–	Fe^{3+} impurities on tetrahedral sites [23]
685	–	355–356	–	Fe^{3+} impurities on tetrahedral sites [21,22]
697	696	355–356	6.3	Fe^{3+} impurities on tetrahedral sites [21,22]

Taking into account that the low content of Ti cations in the starting composition and that impurity centers such as transition metal elements (like Ti^{4+}) and rare-earth elements have narrower bandwidths than those created by defect centers, it can be concluded that the broad blue emissions observed in the glass-ceramic are mainly attributed to Al-O^--Al centers.

Emissions undergo shifts between both matrices, which might be due to the different crystal fields because of differences in crystallinity, which strongly affects luminescence [33]. It is observed that all emissions are much more intense in the glass-ceramic material, up to 18 times for emissions related to [AlO_4/alkali$^+$] or [AlO_4]^0 and up to 14 times for Al-O^--Al linkages, than in the thermally treated mineral. Differences in structure, microstructure, and crystallinity between the rare-earth-free glass-ceramic and the thermally treated mineral might be responsible for the enhancement of luminescence behavior displayed in Fig. 1. For this reason, a structural analysis is carried out hereafter.

B. Structural and Microstructural Study: XRD, FESEM, and TEM Study

Figure 2(a) shows the XRD pattern for the glass-ceramic, which indicates the major phase formation of a plagioclase in the glass-ceramic. XRD pattern may correspond to a Na-rich plagioclase (JCPDS Card no. 00-041-1480) or a calcium-rich (Ca-rich) plagioclase (JCPDS Card no. 00-041-1481). On account of the similarity of both XRD patterns and the overlapping of XRD peaks, it cannot be precisely identified by this technique if the major phase is sodium (albite) or CA-rich (anorthite) feldspar. However, Raman spectroscopy is a suitable tool for such purpose, since it does allow discriminating between phases in alkali feldspars [34]. The Raman spectrum of the micro-nanostructured glass-ceramic, taken on a microcrystal, is illustrated in Fig. 2(b). The two main Raman modes, typical of Raman spectra for feldspars, are those labelled as ν_a and ν_b in Fig. 2(b). Bersani *et al.* [35] have recently reported that the difference between peak position of ν_a and ν_b ($\Delta\nu_{ab} = \nu_a - \nu_b$) delimit the content of anorthite present in the samples. Samples with $\Delta_{ab} > 27$ cm^{-1} have an anorthite content <60 mol.%. In our case, $\Delta_{ab} = 32$ cm^{-1}, and therefore anorthite content is <60 mol.%. By comparison with spectral features of other plagioclases reported in literature [34,35], it is confirmed that the major phase of the micro-nanostructured glass-ceramic is a Na-rich plagioclase phase, and henceforth, it will be referred as Na-rich plagioclase-based glass-ceramic. The presence of SrO in the precursor frit (Table 1) permits the formation of the Na-rich plagioclase phase during the fast-sintering process by the devitrification process, although the frit only has a 2% of Na_2O [18]. In Fig. 2(a), it is also included the diffraction pattern of the raw and the thermally

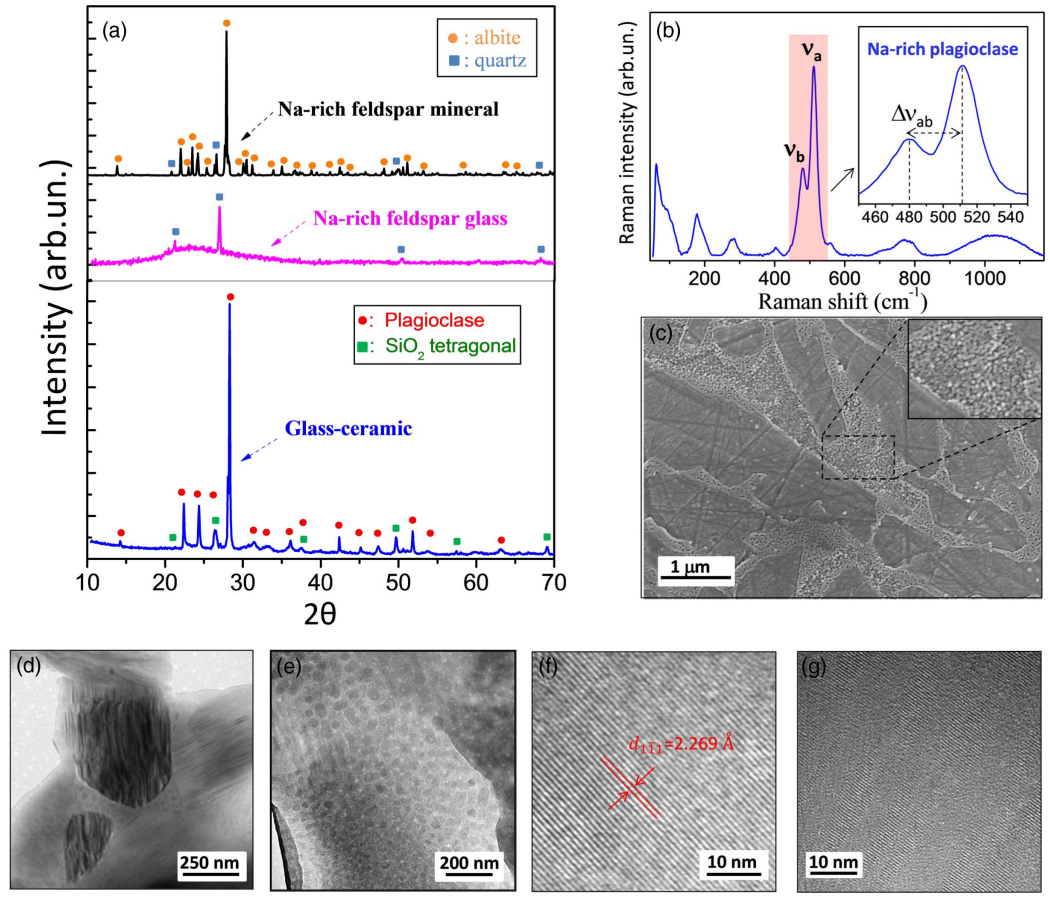

Fig. 2. Structural, microstructural, and morphological characterization of glass-ceramic and mineral Na-rich feldspar: (a) XRD pattern for Na-rich feldspar mineral (in black), Na-rich feldspar glass (in pink), and the glass-ceramic (in blue); (b) Raman spectrum of the glass-ceramic showing that Na-rich plagioclase is the major phase; (c) FESEM micrograph for glass-ceramic showing the presence of large microcrystals almost isolated by nanostructured regions; (d) TEM micrograph showing stripped patterns of microcrystals in addition of the appearance on nanocrystals in the nanostructured regions; (e) detailed presence of nanocrystals embedded in a glass matrix in the nanostructured regions; (f) HRTEM micrograph of a selected region in microcrystal with high crystallinity; and (g) HRTEM micrographs of microcrystals showing crystalline modulation of the interplanar spacing.

treated Na-rich feldspar mineral. The XRD pattern of the raw Na-rich feldspar mineral has a crystalline structure, which agrees with reflections of JCPDS Card no. 01-074-0603 that correspond to a low albite sample, although reflections appear slightly shifted to lower 2θ (see Fig. S3 in Supplement 1), which might be due to the presence of calcium and potassium in the structure (see Table 1), forming a ternary feldspar with albite as major phase. A shift to lower 2θ in the XRD pattern [36] is observed for the Na-rich feldspar mineral, since ionic radius of Ca^{2+} and K^{+} cations are higher than the one corresponding of Na^{+} cation. The incorporation of such cations in albite structure produces a crystal cell expansion. This fact justified the lack of luminescence in the raw mineral. However, when the raw mineral is thermally treated, a Na-rich feldspar glass is formed (and named as Na-rich feldspar glass henceforth), presenting a broad halo at low angles, characteristic of vitreous materials and some crystalline peaks corresponding to quartz phase, as can be seen in Fig. 2(a).

Both thermally treated materials are based on sodium aluminosilicate having quite a different crystallinity degree. Up to 1 magnitude order enhancement in luminescence emission may be originated by different factors: crystallinity, structure, and microstructure [17]. From the XRD pattern of glass-ceramic [Fig. 2(a)], the average crystallite size and the glassy phase content are determined, being 52 nm and only 6 vol. %, respectively [18], Crystallinity plays a very important role because, in glassy phase, there are many point defects that generate trapping sites and nonradiative recombinations as consequence, which will lead to lower luminescence [8,9]. The Na-rich feldspar glass possesses much more content of glassy phase than the glass-ceramic (about 55 vol. %), which might explain why the luminescent performance exhibited in the rare-earth-free glass-ceramic is higher. Moreover, structure and/or the microstructure of the Na-rich plagioclase-based glass-ceramic can be responsible of enhancement in luminescence.

From a mineralogical point of view, the glass-ceramic may be considered as an intermediate albite with high degree of Si–Al disorder [37]. The basic cell unit of its triclinic structure consists of rings of four tetrahedra [four symmetrically nonequivalent sites, designated as $T_1(0)$, $T_1(m)$, $T_2(0)$, and $T_2(m)$] [37,38]. As calcium content increases anorthite content, migration of Al^{3+} cations from $T_1(0)$ positions to $T_1(m)$, $T_2(0)$, and $T_2(m)$ positions might increase, regarding a low albite feldspar to obtain the local charge balance. Anorthitic structures are energetically more favorable for an Si–Al ordered structure. In contrast, when in albite the formation of Al-O^{-}-Al bridges is favoured, and therefore the structure is more likely to be disordered [13,35]. Besides, the presence of different Al^{3+} tetrahedral positions favor their substitution by Fe^{3+} impurities, which causes the increase of red luminescence [Fig. 1(d)]. Thus, first, it can be established that structure might play a key role in the enhancement of luminescence.

In the case of the Na-rich feldspar glass, luminescence comes from tetrahedral ring distortion, which is also presented in the glassy phase but not in an ordered arrangement at large scale, as in the glass-ceramic.

Figure 2(c) shows a FESEM micrograph of the rare-earth-free glass-ceramic having a unique dual microstructure, with elongated Na-rich plagioclase microcrystals surrounded by nanostructured regions that isolate microcrystals. However, the Na-rich feldspar glass does not have any microstructure due to its vitreous nature. A depth TEM analysis of the glass-ceramic feldspar [Figs. 2(d) and 2(e)] showed in detail the nanostructured region between two microcrystals. In these two microcrystals, it can be observed a striped pattern of ∼175–500 nm in width, alternating clear and dark zones. The difference in contrast in such microcrystals indicates compositional differences. These modulations resemble the spinodal decomposition, which is characteristic of some in feldspar minerals [39,40]. To the best of authors' knowledge, this has never been reported for synthetic plagioclases. Spinodal decomposition is used in different materials to enhance their properties, which may open a new research line in feldspar synthetic materials in order to look for new properties derived from such modulations [41,42]. Figure 2(e) shows a nanostructured region of the glass-ceramic having nanocrystals with an average diameter between 30–40 nm. A HRTEM image of Fig. 2(f) is performed on a microcrystal, according to the microstructure depicted in Fig. 2(c). It can be observed that is totally crystalline with three crystallographic directions presented, according to the spots of the corresponding FFT pattern (see Fig. S2a in Supplement 1). The indexing process allows identifying these spots with $(1\bar{5}2)$, $(2\bar{2}0)$, and $(11\bar{2})$ planes, which correspond to interplanar distances of 0.1840 nm, 0.3150 nm, and 0.3570 nm, respectively. These values are slightly different from those tabulated for albite, i.e., 0.1844 nm for $(1\bar{5}2)$, 0.3148 nm for $(2\bar{2}0)$, and 0.3504 nm for $(11\bar{2})$ [43]. This fact is supported by the presence of calcium and strontium in the composition, which may cause the distortion of the Na-rich plagioclase structures regarding the albite structure and consequently distortion in some crystallographic directions. Apart from these regions characterized by their crystallinity and homogeneity, there are some spinodal modulation regions where some crystallinity modulations are observed, as the HRTEM image of Fig. 2(g) depicts. The FFT pattern of this HRTEM image (see Fig. S2b in Supplement 1) reveals the presence of the (202) plane, which corresponds to an interplanar distance of 0.2006 nm [43] and the $(1\bar{1}1)$ plane. The latter exhibits a widened spot, which corresponds to interplanar spacing from 0.3824 nm to 0.3940 nm, indicating a slight gradual compositional variation. An inversed image of the $(1\bar{1}1)$ spot (see Fig. S2c in Supplement 1) revealed that this compositional modulation is composed of alternate crystalline and noncrystalline regions.

This unique micro-nanostructure is originated from both the formation process and the composition. As consequence, the enhanced luminescence seems to have a strong dependence on such crystal modulations. In order to deepen this study and evaluate the influence of the micro-nanostructure in the enhancement of the luminescence of this new synthetic material, the importance of the nanostructuration in the luminescence emission is studied by means of quenching experiments. Luminescent nanoparticles present quantum confinement effects, which leads to novel optoelectronic properties. However, nanosized phosphors usually have a larger defect number because of a larger surface-to-volume ratio, which sometimes leads to a decrease of quantum efficiency [3].

In the micrographs of Figs. 3(a)–3(c) (and Figs. S5a–S5c in Supplement 1), it might be observed the evolution of the glass-ceramic microstructure for different thermal treatments. At 1100°C [Figs. 3(a) and S5a], large isolated microcrystals in a glass matrix are formed. For quenched samples at 1220°C [Figs. 3(b) and S5b], nanocrystals nucleate at the glassy phase but are agglomerated and not well formed yet. However, it is during the cooling when the nanostructure comes to settle the whole sample, isolating microcrystals between each other [Figs. 3(b)–3(c) and S5

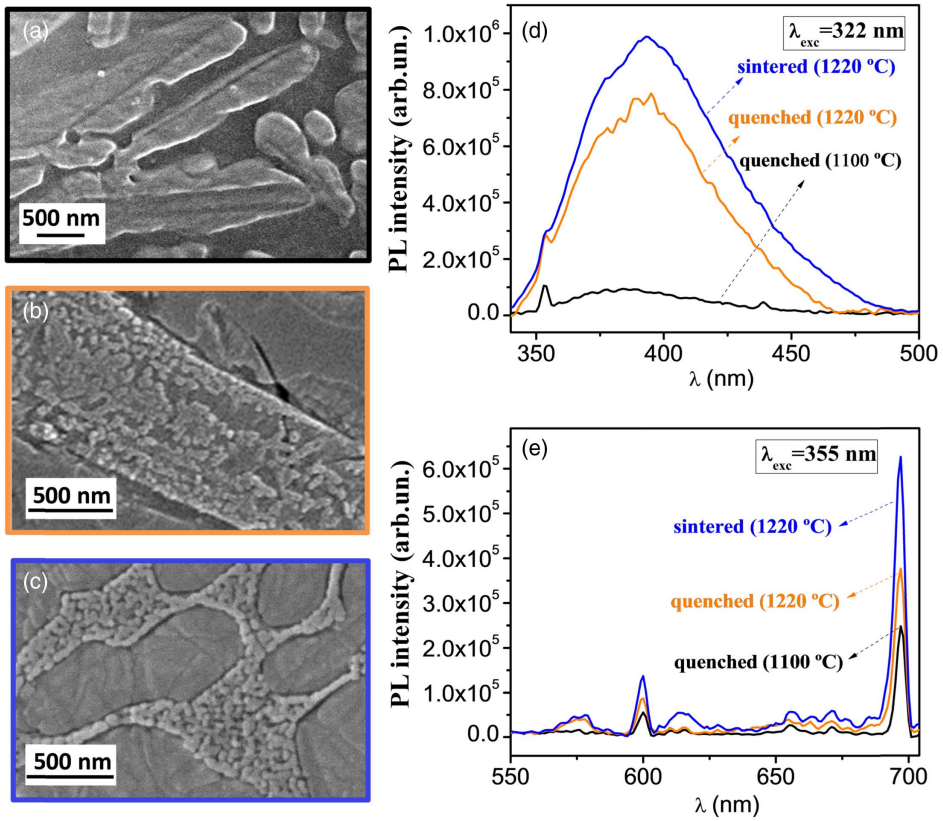

Fig. 3. Processing dependence of luminescence in glass-ceramics: FESEM micrographs for glass-ceramic for different thermal treatments: (a) 1100°C and quenched, (b) 1220°C and quenched, and (c) 1220°C and slow cooled. Emission spectra for glass-ceramic thermally treated at 1100°C and quenched (in black), at 1220°C and quenched (in orange), and at 1220°C and slow cooled (in blue) are showed for different excitation wavelengths: (d) $\lambda_{exc} = 322$ and (e) $\lambda_{exc} = 355$ nm.

b–S5c]. Figure S6 of Supplement 1 shows the XRD pattern for these three samples. At 1100°C, the plagioclase crystallization has already produced, and it is possible to observe the well-defined XRD pattern, with a very low amount of glassy phase. In addition, tetragonal SiO_2 also appears. For the quenched sample at 1220°C, the XRD pattern is very similar to the one quenched at 1100°C; however, the diffraction peak intensities increases, which indicates higher crystallinity. Finally, in the XRD pattern of the sample sintered at 1220°C for 6 min, the Na-rich plagioclase diffraction pattern with higher crystallinity can be observed.

Figures 3(d) and 3(e) depict the luminescence emission under an excitation at 322 nm and 355 nm, respectively. At 322 nm, structural defects of the glass-ceramic are the main responsibility of the emission. In this case, band emission at ~350–500 nm considerably rises as nanostructuration is formed. The luminescence intensity increases up to 1 magnitude order when the glassy region transforms in a nanostructure region in glass-ceramic feldspar sintered at 1220°C and slowly cooled. It is also illustrated as a general feature, that the enhancement of luminescent is correlated with the appearance of nanostructured regions. The development of a dual microstructure is a key factor for such micronanostructural evolution. However, it may be taking into account that the nanocrystal region occurs in the presence of microcrystal that shows compositional modulations, that is, the plagioclase structure is defective.

Fe^{3+} as well as some emissions related to quartz are excited at 355 nm. Red emission placed at 697 nm increases around 1.5 times when the nanostructure starts to appear (quenched at 1220°C) and 2.5 times when all the micro-nanostructure is developed (sintered at 1220°C) regarding when only Na-rich plagioclase microcrystals are presented in the sample (quenched at 1100°C). Red luminescence improvement with the micro-nanostructure is less noticeable than UV–blue emission, which suggests that structural defects such as Al-O^--Al linkages and alkali cations placed adjacent to Al^{3+} cations evolved during the slow cooling as consequence of almost complete devitrification of the glass-ceramic feldspars.

C. Cathodoluminescence Reveals the Appearance of Luminescence in Fast-Sintered Glass-Ceramics

CL coupled to a SEM microscope for fast-sintered glass-ceramic is presented in Fig. 4. Although the SEM resolution in Fig. 4(a) is not as high as in FESEM micrographs, Fig. 2 and 3, the main features of the elongated microcrystals almost isolated in a matrix are observed. The micrograph resolution does not resolve the nanoparticles in the matrix, but the location of such regions are well defined in previous FESEM measurements, being between microcrystals. Therefore, measurements in these two regions were carried out.

Figure 4(b) shows an average SEM-CL spectrum for both the microcrystal and the nanocrystals regions. The spectra are measured from 250 to 800 nm in order to compare both CL emissions. CL intensity for nanocrystals is slightly lower than for microcrystals, which might be associated by a larger scattering of the nanoregions because of a larger surface-to-volume ratio.

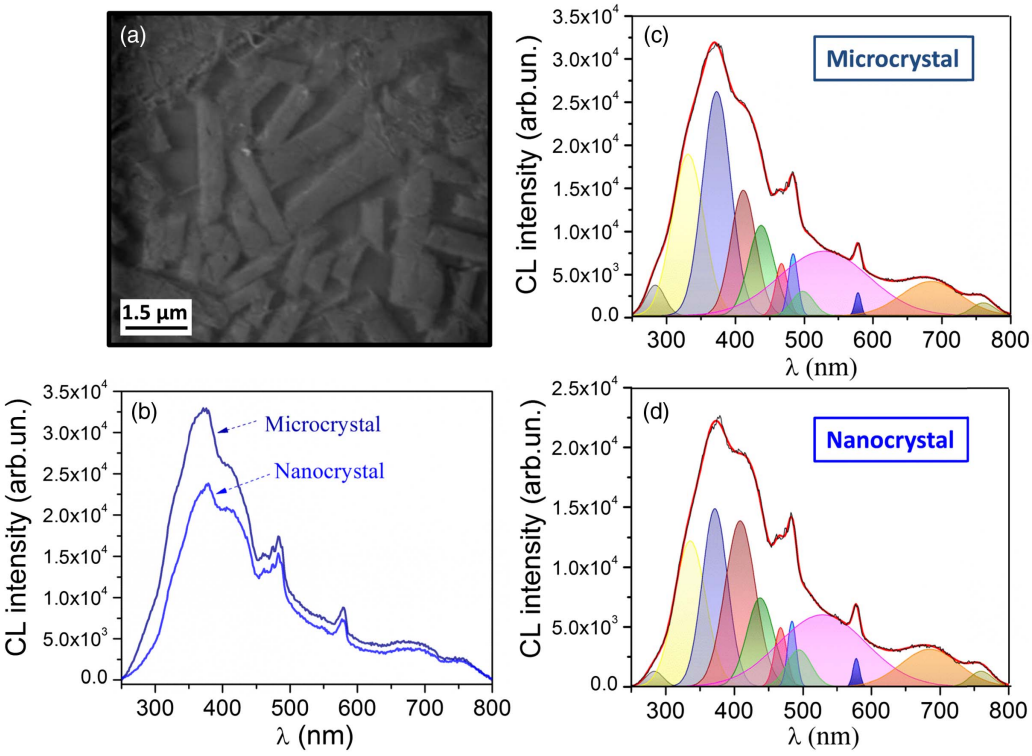

Fig. 4. Microscopic analysis of the cathodoluminescence occurrence: (a) SEM-CL micrograph of micro-nanostructured fast-sintered glass-ceramic; (b) characteristic SEM-CL spectra for microstructured and nanostructured regions; and (c), (d) the corresponding deconvolutions of CL spectra for microcrystals and nanocrystals, respectively, showing different emission bands associated with defects tabulated in Table 3.

The deconvolution of both spectra is plotted in Figs. 4(c) and 4(d). The emission peaks obtained from the deconvolution of the CL curve for nanocrystals and microcrystals are similar, and they are summarized in Table 3. However, some wavelength shifts between them are observed, as well relevant differences in the area contribution of some of the emission peaks (Table 3).

The glass-ceramic presents several emission peaks that correspond to structural defects such as Al-O^--Al bond and [AlO_4/alkali$^+$] or [AlO_4]^0 centers. The first emission peak at around 284 nm is a UV emission that has been reported for high albite plagioclases, which is probably caused by a defect site associated with a sodium feldspar lattice structure [28]. Additionally, emission peaks at ca. 331 nm and ca. 336 nm may be associated with strained Si–O bonds in feldspars [44,45]. The presence of hole trapped in nonbridging oxygen or Si–O bond defects can be responsible for these UV emissions [44,45]. The UV luminescence emissions at ca. 372 nm and ca. 373 nm are the most intense ones and are described as [AlO_4/alkali] or [AlO_4]^0 centers. Emissions in the range of 409–484 nm are mainly attributed to Al-O^--Al defect centers [22,26–29]. However, according to the low spectral contribution displayed in Figs. 4(c) and 4(d) [26,29], the emission bands at ca. 466 nm for microcrystals and ca. 465 nm for nanocrystals could be also related to Ti centers. The emissions peaks in the range of 494–529 nm are probably associated with a hole on oxygen adjacent to a divalent impurity (Si – O^-…M^{2+}), as it was suggested that this kind of center is

Table 3. Assignment of the Main Emission Peaks: CL Emission Peak Positions of Deconvoluted Spectra for Microcrystals and Nanocrystals in the Glass-Ceramic[a]

λ_{micro} (nm)	λ_{nano} (nm)	$Area_{nano}/Area_{micro}$	Assignment
284	284	0.5	defect site in a Na-feldspar lattice structure [28]
331	336	0.9	defects in Si–O strained structures [44,45]
373	372	0.7	[AlO_4/alkali$^+$] or [AlO_4]^0 [20,22]
412	409	1.6	Al-O^--Al center [2627–28]
437	438	1.0	Al-O^--Al center [29,26]
467	467	1.1	Ti or Al-O^--Al center [29,26]
484	484	1.0	Al-O^--Al center [29,26]
498	494	1.7	Si-O^-…M^{2+} with M = Mg or Zn [11]
529	529	1.1	Si-O^-…M^{2+} with M = Mg or Zn [11]
578	578	1.3	oxygen vacancies in quartz [30]
684	685	1.1	$Fe^{3+} \rightarrow Fe^{2+}$ impurities [21,22]
760	760	1.2	Fe^{3+} impurities on T_1 sites [26]

[a]The $Area_{nano}/Area_{micro}$ ratio and the emission peak assignments according to referenced defect are also summarized.

stabilized by a divalent metal ion, M^{2+}, in a T site adjacent to the oxygen [11]. The most likely cations are Sr^{2+}, Mg^{2+}, or Zn^{2} according to the glass-ceramic chemical composition [11,19]. Emission peak at ca. 578 nm is assigned to oxygen vacancies in a quartz-type structure [30]. Emissions peaks at ca. 684 nm and ca. 685 nm, corresponding to Fe^{2+} cations, are consequence of the irradiation with a high-energy electron, accelerated at 30 keV, that reduces Fe^{3+} cations into Fe^{2+} cations. Additionally, emission peaks at ca. 684 nm and ca. 685 nm can be related to lattice defects, such as broken Si–O bonds [46]. Finally, red emissions at 760 nm are assigned to Fe^{3+} cations in Al^{3+} tetrahedral sites, probably in $T_1(0)$ positions, as is found in other albite-rich feldspars [26].

As well, main CL emissions registered are quite broad, which indicates that the electron transitions occur in energy levels, which are influenced by the local crystal field. The wavelength shifts observed in some emission peaks for the microstructure and nanostructure regarding each other revealed the strong influence of the host crystal. The fast-sintered glass-ceramic generate structural strains according with the micro-nanostructure analysis that the revealed regions have variation of alkali–alkaline earth cations, which modulated the crystal field in the material. These modulations of the crystal field are on the origin of the enhancement of luminescence emission measured [24,47]. The area ratio between nanocrystals and microcrystals for each CL peak is presented in Table 3. The most relevant contributions are related to intrinsic oxygen defects such as Löwenstein bridges or Si-O^{-}…M^{2+} defects, which possess a more considerable weight in the emissions of the nanocrystal regions than in the microcrystal emissions. These oxygen defects seem to be a clear distinctive between both parts, which may indicate that charge might be accumulated preferentially in nanostructured regions instead of microcrystals. Defects related to [AlO_4/$alkali^{+}$] or $[AlO_4]^0$ centers (∼ 372–373 nm) are also remarkable, and their contribution in microcrystals is more relevant than in nanocrystal regions, and finally, structural defects at ca. 331 nm for microcrystals and ca. 336 nm for nanocrystals are also relevant luminescent centers. The defects related to impurities as Fe cations show also a higher contribution to the luminescence. The recombinative centers created by Fe cations give a considerable red emission, being also somewhat higher for nanocrystals than for microcrystals.

To sum up, microcrystals and nanocrystal regions contribute similarly to luminescence of this rare-earth-free glass-ceramic, although they present a different density of defects. Therefore the hypothesis that nanostructured areas may responsible for the luminescence enhancement is not supported. The CL analysis revealed that both the micro and the nanoregions contributed the enhancement of the luminescence in comparison with feldspar glass.

D. NMR Study: Identification of Structural Defects Responsible for Luminescence in Fast-Sintered Glass-Ceramics

The presence of Si–Al disorder, Al-O^{-}-Al bonds, and alkali cations adjacent to Al^{3+} cation is responsible in feldspar glass-ceramics for enhancement of luminescence emissions. In order to stablish if a correlation exists between Si–Al disorder and the defects, NMR measurements are carried out. Figure 5 shows the ^{29}Si NMR spectrum for the precursor frit [Fig. 5(a)] and the micro-nanostructured glass-ceramic [Fig. 5(b)], whose analysis allows obtaining information about electronic environment around Si sites.

^{29}Si NMR spectrum of the frit [Fig. 5(a)] exhibits a broad band, from −65 to −125 ppm approximately with a maximum at ∼ − 92 ppm. The different polymerization state in which silicon is found in the vitreous network of the precursor frit might be inferred from the deconvolution of it spectrum. ^{29}Si NMR peaks are tabulated in Table 4 in addition to the area contribution of each band and the corresponding Qn assignment. According to bibliography [48,49], chemical shift values from −66 ppm to −74 ppm are assigned to Q0 units in the ^{29}Si NMR spectrum. Bands in the range of −82 to −75 ppm correspond to Q1 units, and in the range of −86 to −84 ppm correspond to Q2 units. Q3 units appear in the range of −101 to −90 ppm while Q4 groups provide bands in the range from −120 to −103 ppm. Q3 species are the major contribution with around 86% of the total area, as indicated in Table 4.

The deconvoluted ^{29}Si NMR spectrum for the micro-nanostructured glass-ceramic is shown in Fig. 5(b). Chemical shift peaks tabulated at −71.0 ppm and −66.7 ppm might be associated to Q_0 units, peaks at −79.3 ppm and −75.4 ppm correspond to Q_1 units, and peaks at −109.4 ppm to Q_4 units, all of them arising from the parent glass. The small quantity of glassy phase in the highly crystalline glass-ceramic, previously discussed by XRD measurements, is also evinced by NMR, because of the small area contribution of these associated bands. The other peaks mainly correspond to Q_4 units of the Na-rich plagioclase with the exception of the peak located at ∼ − 85 ppm, which is associated to Q_4(4Al), characteristic of anorthite-like sites [50,51]. The peak at ∼ − 89 ppm may be associated to T_2(3Al) site of albite structure,

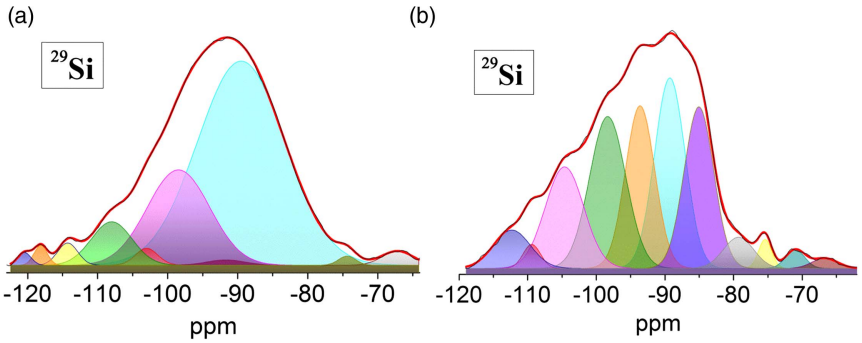

Fig. 5. Structural evolution of ^{29}Si NMR spectra with crystallization: (a) the precursor frit and (b) the micro-nanostructured glass-ceramic sintered at 1220°C and slow cooled. Deconvolution of ^{29}Si NMR spectrum in different chemical shift peaks is shown by colored peaks indicating a different polymerization state of Q_n units (assignment of chemical shift peak is summarized in Table 4).

Table 4. Assignments of Deconvoluted ^{29}Si NMR Spectrum: Chemical Shift (ppm), Area Contribution (%), and Assignment for Each Deconvoluted Band of the ^{29}Si NMR Spectrum for the Precursor Frit and the Micro-Nanostructured Glass-Ceramic Sintered at 1220°C and Slow Cooled[a]

Precursor Frit			Micro-Nanostructured Glass-Ceramic		
Chemical Shift (ppm)	Area Contribution (%)	Q_n Unit Assignment	Chemical Shift (ppm)	Area Contribution (%)	Site Assignment
−67.1	1.6	Q_0	−66.7	0.9	Q_0 unit (glass)
−73.9	0.6	Q_0	−71.0	1.2	Q_0 unit (glass)
−89.5	64.5	Q_3	−75.4	1.3	Q_1 unit (glass)
−91.7	0.7	Q_3	−79.3	3.3	Q_1 unit (glass)
−98.5	21.6	Q_3	−85.0	16.8	Q_4(4Al) (*)
−103.0	1.4	Q_4	−89.3	20.5	T_2 (3Al)
−108.0	6.4	Q_4	−93.6	16.7	T_{2m} (2Al)
−114.3	1.6	Q_4	−98.3	19.2	T_{20} (1Al)
−118.1	1.0	Q_4	−104.6	13.7	T_{1m} (1Al)
−120.5	0.6	Q_4	−109.4	1.5	Q_4 unit (glass)
–	–	–	−112.3	4.9	T_1 (0Al)

[a]Area contribution shows that Q_3 species are the major one in the precursor frit and Q_4 species are the major one in the case of glass-ceramic. (*) indicates an anorthite-like site. The rest of tabulated positions between −112.3 ppm to −89.3 ppm correspond to albite-like sites.

typically placed in the range from −91 to −87 ppm in plagioclases [51]. The rest of peaks located at −112.3, −104.6, −98.3, and −93.6 ppm match well with albite-like sites corresponding to T_1(4Si, 0Al) T_1m(3Si, 1Al), T_{20}(3Si, 1Al), and T_{2m}(2Si, 2Al) positions, respectively [50–52]. Chemical shifts registered for the synthetic glass-ceramic slightly differ from reported values in bibliography for natural minerals, as occurred with luminescence emission. This fact is due to the presence of different elements such as calcium, strontium, and in lesser extent potassium, which act as lattice disruptors in the Na-rich plagioclase structure regarding a pure albite and consequently change bond distances and resonances.

In a low albite, the most ordered kind of albite, Si is placed in $T_1(m)$, $T_2(0)$, and $T_2(m)$ sites while Al in $T_1(0)$ and the corresponding ^{29}Si NMR spectrum exhibit three bands of equal intensity [51]. However the ^{29}Si NMR spectrum of the rare-earth-free glass-ceramic [Fig. 5(b)] presents more bands, with different width and intensity and even overlapping each other, which indicates that Si neighbors have considerably changed with regard to an ordered state [53]. Moreover, the presence of T_2(3Al) and T_1(0Al) sites in albite-like domains corroborate that a Si–Al disorder distribution is presented. It can be stablished a perfect correlation between Si–Al disorder and formation of luminescent centers, such as Al-O$^-$-Al bonds and alkali adjacent to Al^{3+} tetrahedra, which has been proved to be crucial to display an enhanced luminescent behavior. In addition, the high crystallinity of the glass-ceramic regarding the Na-rich feldspar glass favors this luminescent enhancement. Therefore, structure carried out a decisive role in such improvement of luminescence while microstructure is related to the processing that modulated such structure. The occurrence of two devitrification steps, first the appearance at 1100°C of microcrystal and second the nucleation of nanocrystal at 1220°C that extend during the slow cooling process are responsible to keep such Si–Al disorder. Moreover, the presence of different alkaline and alkaline-earth cations favor both the deformation and interplanar spacing that contribute to the modulations of crystal field.

It is worth mentioning that the strong relation between luminescence and structural disorder in this novel family of rare-earth-free luminescent materials opens the topic toward the tailoring of feldspar structure by incorporating compositional variations or dopants. Further advances in rare-earth-free luminescence materials will be attempted based in inducing structural disorder at long range in feldspar structures and therefore enhancing and tuning the corresponding luminescence emissions.

4. CONCLUSION

Novel rare-earth-free glass-ceramic-based phosphor with high luminescence has been designed by a scalable approach based on a conventional ceramic process. This novel phosphor is rich in Na-plagioclase feldspar crystallizations and presents high crystallinity, ∼94%, along with a unique micro-nanostructure developed by a fast-sintering process. TEM and HRTEM analyses reveal the coexistence of compositionally homogeneous microcrystals and some others, which present compositional inhomogeneities, manifested by spinodal decomposition modulations.

In this work, luminescence of a novel rare-earth-free glass-ceramic based on feldspar crystallizations has been deeply studied for the first time, to the best of our knowledge. CL, ^{29}Si NMR measurements, and quenching experiments show that structure has a key role in the luminescence behavior of this novel phosphor. Structural disorder in Si–Al distribution favors the formation of several luminescent centers, namely, Al-O$^-$-Al bonds, [AlO_4/alkali$^+$] and $[AlO_4]^0$, that result in an increase of 1 magnitude order in the broad UV–blue PL emission exhibited and around 6 times in the red luminescence regarding a Na-rich feldspar glass obtained from a mineral source. Moreover, the high crystallinity of the glass-ceramic also favors such luminescent enhancement.

It should be noticed that the results obtained in this work for a new class of micro-nanostructured rare-earth-free phosphors can be considered as a reference for future works in this research topic, since through a suitable compositional modification, a rise of structural disorder may be obtained. Consequently, luminescent emissions could be tuned and increased. Further advances in glass-ceramic feldspar to improve its luminescence behavior would be technologically very relevant for applications such as security markers or light-emitting glasses.

Funding. Ministerio de Economía y Competitividad (MINECO) (MAT2017-86450-C4-1-R, PTQ- 14-07289).

Acknowledgment. The authors express their thanks to B. Galiana and M. J. De la Mata for their contributions in carrying out TEM and NMR measurements, respectively.

See Supplement 1 for supporting content.

REFERENCES

1. C. Feldmann, T. Jüstel, C. R. Ronda, and P. J. Schmidt, "Inorganic luminescent materials: 100 years of research and application," Adv. Funct. Mater. **13**, 511–516 (2003).
2. D. Ehrt, "Photoluminescence in glasses and glass ceramics," IOP Conf. Ser. Mater. Sci. Eng. **2**, 012001 (2009).
3. R. E. Rojas-Hernandez, F. Rubio-Marcos, A. Serrano, A. D. Campo, and J. F. Fernandez, "Precise tuning of the nanostructured surface leading to the luminescence enhancement in $SrAl_2O_4$ based core/shell structure," Sci. Rep. **7**, 1–9 (2017).
4. P. G. G. Slaats, G. J. Dirksen, and G. Blasse, "Luminescence of some activators in synthetic potassium feldspar crystals," Mater. Chem. Phys. **30**, 19–23 (1991).
5. M. Karbowiak, A. Mech, A. Bednarkiewicz, W. Stręk, and L. Kępiński, "Comparison of different $NaGdF_4$:Eu^{3+} synthesis routes and their influence on its structural and luminescent properties," J. Phys. Chem. Solids **66**, 1008–1019 (2005).
6. N. C. George, K. A. Denault, and R. Seshadri, "Phosphors for solid-state white lighting," Annu. Rev. Mater. Res. **43**, 481–501 (2013).
7. G. Boulon, "Luminescence in glassy and glass ceramic materials," Mater. Chem. Phys. **16**, 301–347 (1987).
8. M. Nikl, J. A. Mares, E. Mihokova, K. Nitsch, N. Solovieva, V. Babin, A. Krasnikov, S. Zazubovich, M. Martini, A. Vedda, P. Fabeni, G. P. Pazzi, and S. Baccaro, "Radio- and thermoluminescence and energy transfer processes in Ce^{3+}(Tb^{3+})-doped phosphate scintillating glasses," Radiat. Meas. **33**, 593–596 (2001).
9. G. P. Pazzi, P. Fabeni, C. Susini, M. Nikl, E. Mihokova, N. Solovieva, K. Nitsch, M. Martini, A. Vedda, S. Baccaro, A. Cecilia, and V. Babin, "Defect states induced by UV-laser irradiation in scintillating glasses," Nucl. Instrum. Methods Phys. Res. Sect. B **191**, 366–370 (2002).
10. O. Dymshits, M. Shepilov, and A. Zhilin, "Transparent glass-ceramics for optical applications," MRS Bull. **42**(3), 200–205 (2017).
11. D. Barbin, V. Pagel, M. Blanc, and P. Ohnenstetter, *Cathodoluminescence in Geosciences* (Springer, 2000).
12. A. S. Marfunin, *Spectroscopy, Luminescence and Radiation Centers in Minerals* (Springer, 1979).
13. A. Putnis, "The crystal structure of minerals II—silicates," in *An Introduction to Mineral Sciences* (Cambridge University Press, 1992), pp. 141–184.
14. J. E. Contreras and E. A. Rodríguez, "Nanostructured insulators—a review of nanotechnology concepts for outdoor ceramic insulators," Ceram. Int. **43**, 8545–8550 (2017).
15. X. Cui, Y. Cheng, H. Lin, F. Huang, Q. Wu, and Y. Wang, "Size-dependent abnormal thermo-enhanced luminescence of ytterbium-doped nanoparticles," Nanoscale **9**, 13794–13799 (2017).
16. G. H. Beall and L. R. Pinckney, "Nanophase glass-ceramics," J. Am. Ceram. Soc. **82**, 5–16 (1999).
17. N. Joffin, J. Dexpert-Ghys, M. Verelst, G. Baret, and A. Garcia, "The influence of microstructure on luminescent properties of Y_2O_3:Eu prepared by spray pyrolysis," J. Lumin. **113**, 249–257 (2005).
18. V. Fuertes, M. J. Cabrera, J. Seores, D. Muñoz, J. F. Fernández, and E. Enríquez, "Hierarchical micro-nanostructured albite-based glass-ceramic for high dielectric strength insulators," J. Eur. Ceram. Soc. **38**, 2759–2766 (2018).
19. E. Enríquez, V. Fuertes, M. J. Cabrera, J. Seores, D. Muñoz, and J. F. Fernández, "New strategy to mitigate urban heat island effect: energy saving by combining high albedo and low thermal diffusivity in glass ceramic materials," Sol. Energy **149**, 114–124 (2017).
20. J. Garcia-Guinea, P. D. Townsend, L. Sanchez-Munoz, and J. M. Rojo, "Ultraviolet-blue ionic luminescence of alkali feldspars from bulk and interfaces," Phys. Chem. Miner. **26**, 658–667 (1999).
21. Y. Kirsh and P. D. Townsend, "Speculations on the blue and red bands in the TL emission spectrum of albite and microcline," Int. J. Radiat. Appl. Instrum. Part D **14**, 43–49 (1988).
22. V. Correcher, J. Garcia-Guinea, L. Sanchez-Muñoz, and T. Rivera, "Luminescence characterization of a sodium-rich feldspar," Radiat. Eff. Defects Solids **162**, 709–714 (2007).
23. M. Ostrooumov, *Amazonite : Mineralogy, Crystal Chemistry, and Typomorphism* (Elsevier, 2016).
24. M. R. Krbetschek, J. Götze, G. Irmer, U. Rieser, and T. Trautmann, "The red luminescence emission of feldspar and its wavelength dependence on K, Na, Ca—composition," Mineral. Petrol. **76**, 167–177 (2002).
25. W. J. Rink, H. Rendell, E. A. Marseglia, B. J. Luff, and P. D. Townsend, "Thermoluminescence spectra of igneous quartz and hydrothermal vein quartz," Phys. Chem. Miner. **20**, 353–361 (1993).
26. M. Kayama, S. Nakano, and H. Nishido, "Characteristics of emission centers in alkali feldspar: a new approach by using cathodoluminescence spectral deconvolution," Am. Mineral. **95**, 1783–1795 (2010).
27. D. J. Huntley, D. I. Godfrey-Smith, and E. H. Haskell, "Light-induced emission spectra from some quartz and feldspars," Int. J. Radiat. Appl. Instrum. Part D **18**, 127–134 (1991).
28. M. L. Clarke and H. M. Rendell, "Infra-red stimulated luminescence spectra of alkali feldspars," Radiat. Meas. **27**, 221–236 (1997).
29. S. Maki, S. Ohgo, and H. Nishido, "Cathodoluminescence characterization of feldspar minerals from granite-syenite rocks in Iwagijima Island, Ehime Prefecture, Japan," Naturalistae **538**, S13–S16 (2016).
30. J. Götze, "Defect structure and luminescence behaviour of agate—results of electron paramagnetic resonance (EPR) and cathodoluminescence (CL) studies," Mineral. Mag. **63**(2), 149–163 (1999).
31. M. A. Kasymdzhanov and P. K. Khabibullaev, "Nanosecond duration broadband luminescence of quartz glasses," Turkish J. Phys. **22**, 475–480 (1998).
32. J. Götze, M. Plötze, and D. Habermann, "Origin, spectral characteristics and practical applications of the cathodoluminescence (CL) of quartz—a review," Mineral. Petrol. **71**, 225–250 (2001).
33. L. Wondraczek, S. Krolikowski, and P. Nass, "Europium partitioning, luminescence re-absorption and quantum efficiency in (Sr, Ca) åkermanite–feldspar bi-phasic glass ceramics," J. Mater. Chem. C **1**, 4078–4086 (2013).
34. J. Freeman, E. Kuebler, L. Jolliff, and A. Haskin, "Characterization of natural feldspars by Raman spectroscopy for future planetary exploration," Canad. Mineral. **46**, 1477–1500 (2008).
35. D. Bersani, I. Aliatis, M. Tribaudino, L. Mantovani, A. Benisek, M. A. Carpenter, G. D. Gatta, and P. P. Lottici, "Plagioclase composition by Raman spectroscopy," J. Raman Spectrosc. **49**, 684–698 (2018).
36. V. Fuertes, A. Mariscal, R. Serna, F. J. Mompeán, M. García-Hernández, J. F. Fernández, and E. Enríquez, "Multifunctional ZnO/Fe-O and graphene oxide nanocomposites: enhancement of optical and magnetic properties," J. Eur. Ceram. Soc. **37**, 3747–3758 (2017).
37. V. F. de la Llave, A. del Campo, J. F. Fernández, and E. Enríquez, "Structural insights of hierarchically engineered feldspars by confocal Raman microscopy," J. Raman Spectrosc. (2019) https://doi.org/10.1002/jrs.5556 (early view).
38. I. Aliatis, E. Lambruschi, L. Mantovani, D. Bersani, S. Andó, G. Diego Gatta, P. Gentile, E. Salvioli-Mariani, M. Prencipe, M. Tribaudino, and P. P. Lottici, "A comparison between ab initio calculated and measured Raman spectrum of triclinic albite ($NaAlSi_3O_8$)," J. Raman Spectrosc. **46**, 501–508 (2015).
39. A. Putnis, "Transformation processes in minerals I: exsolution," in *An Introduction to Mineral Sciences* (Cambridge University Press, 1992), pp. 333–384.
40. L. Sánchez-Munõz, A. Del Campo, and J. F. Fernández, "Symmetry constraints during the development of anisotropic spinodal patterns," Sci. Rep. **6**, 1–10 (2016).
41. M. U. Kim, J. P. Ahn, H. K. Seok, E. Fleury, H. J. Chang, D. H. Kim, P. R. Cha, and Y. C. Kim, "Application of spinodal decomposition to produce metallic glass matrix composite with simultaneous improvement of strength and plasticity," Met. Mater. Int. **15**, 193–196 (2009).
42. S. U. Rehman, Q. Jiang, W. Lei, L. He, Q. Tan, Q. Quan, L. Wang, M. Zhong, S. Ma, A. Ul Haq, and Z. Zhong, "Improved microstructure and magnetic properties of Alnico 8 Alloys by B-doping," IEEE Trans. Magn. **54**, 1–6 (2018).
43. L. Van Der Plas, "The x-ray powder patterns of feldspars," in *Developments in Sedimentology* (Elsevier, 1966), Vol. **6**, pp. 211–212.
44. J. Garcia-Guinea, V. Correcher, L. Sanchez-Muñoz, A. A. Finch, D. E. Hole, and P. D. Townsend, "On the luminescence emission band at 340 nm of stressed tectosilicate lattices," Nucl. Instrum. Methods Phys. Res. Sect. A **580**, 648–651 (2007).

45. A. Aparicio and M. Á. Bustillo, "Cathodoluminescence spectral characteristics of quartz and feldspars in unaltered and hydrothermally altered volcanic rocks (Almeria, Spain)," Spectrosc. Lett. **45**, 104–108 (2012).
46. D. K. Richter, T. Götte, and D. Habermann, "Cathodoluminescence of authigenic albite," Sediment. Geol. **150**, 367–374 (2002).
47. J. Götze, "Potential of cathodoluminescence (CL) microscopy and spectroscopy for the analysis of minerals and materials," Anal. Bioanal. Chem. **374**, 703–708 (2002).
48. O. V. Filonenko, V. S. Kuts, M. I. Terebinska, and V. V. Lobanov, "Quantum chemical calculation of ^{29}Si NMR spectrum of silicone dioxide fullerene-like molecules," Chem. Phys. Technol. Surf. **6**, 263–268 (2015).
49. K. J. D. MacKenzie and E. S. Mark, *Multinuclear Solid-State NMR of Inorganic Materials* (Pergamon, 2002).
50. R. J. Kirkpatrick, R. A. Kinsey, K. A. Smith, D. M. Henderson, and E. Oldfields, "High resolution solid-state sodium-23, aluminum-27, and silicon-29 nuclear magnetic resonance spectroscopic reconnaissance of alkali and plagioclase feldspars," Am. Mineral. **70**, 106–123 (1985).
51. R. J. Kirkpatrick, M. A. Carpenter, W. H. Yang, and B. Montez, "^{29}Si magic-angle NMR spectroscopy of low-temperature ordered plagioclase feldspars," Nature **325**, 236–238 (1987).
52. W. H. Yang, R. J. Kirkpatrick, and D. M. Henderson, "High-resolution ^{29}Si, ^{27}Al and ^{23}Na NMR spectroscopic study of Al-Si disordering in annealed albite and oligoclase," Am. Mineral. **71**, 712–726 (1986).
53. L. Sanchez-Muñoz, L. Nistor, G. Van Tendeloo, and J. Sanz, "Modulated structures in $KAlSi_3O_8$: a study by high resolution electron microscopy and ^{29}Si MAS-NMR spectroscopy," J. Electron Microsc. **47**, 17–28 (1998).